DOI: 10.1002/smll.200500113

# Recent Developments in Nanofabrication Using Focused Ion Beams

*Ampere A. Tseng**

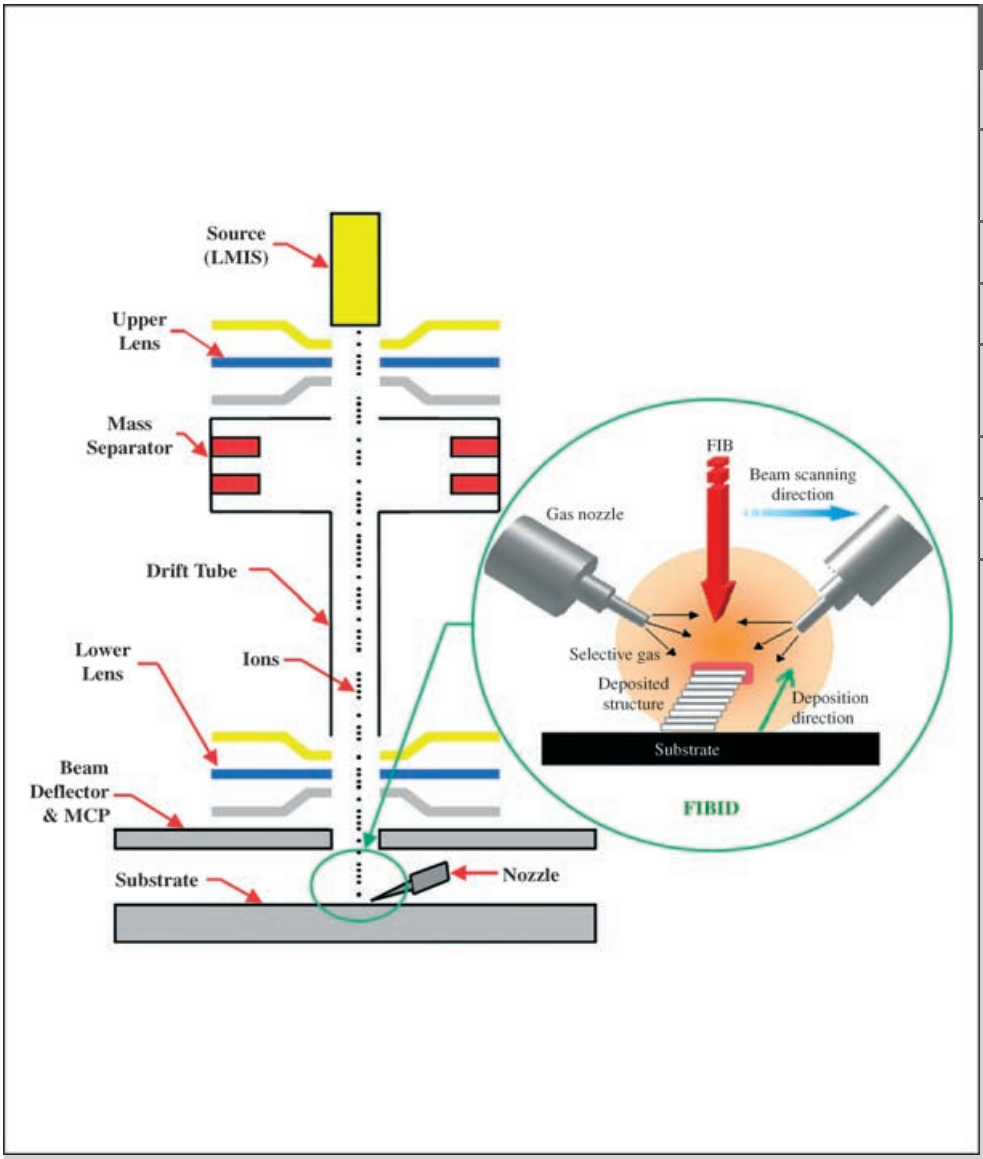


Schematic of a focused ion beam system with a liquid-metal ion source.

NANO MICRO small

## From the Contents

1. Introduction.....*925*
2. Ion Sources and Systems.....*926*
3. Milling.....*926*
4. Implantation.....*931*
5. FIB-Induced Deposition .....*933*
6. FIB-Assisted Etching*935*
7. Concluding Remarks*937*

**Keywords:**
- direct writing
- focused ion beams
- nanofabrication
- nanostructures
- patterning

NANO MICRO small

*Focused ion beam (FIB) technology has become increasingly popular in the fabrication of nanoscale structures. In this paper, the recent developments of the FIB technology are examined with emphasis on its ability to fabricate a wide variety of nanostructures. FIB-based nanofabrication involves four major approaches: milling, implantation, ion-induced deposition, and ion-assisted etching of materials; all these approaches are reviewed separately. Following an introduction of the uniqueness and strength of the technology, the ion source and systems used for FIB are presented. The principle and specific techniques underlying each of the four approaches are subsequently studied with emphasis on their abilities of writing structures with nanoscale accuracy. The differences and uniqueness among these techniques are also discussed. Finally, concluding remarks are provided where the strength and weakness of the techniques studied are summarized and the scopes for technological improvement and future research are recommended.*

## 1. Introduction

Nanofabrication aims at building nanoscale structures, which can act as components, devices, or systems, in large-quantity with potentially low costs (here nanoscale refers to the associated feature sizes in the range from 0.1 to 100 nm). The major benefits for nanofabrication include, but are not limited to, minimizing the use of materials and energy, increasing product resolution and sensitivity, reducing waste and environmental impact, and enabling high-rate, cost-effective production essential to industrial implementation. Recently, focused ion beams (FIBs) have become increasingly popular tools for the fabrication of various types of nanostructures for different applications. In this Review, the capabilities and applications of the FIB technology for nanofabrication are examined.

FIB has several advantages over other high-energy particle beams used in nanofabrication. For example, when compared to electrons, ions are much heavier and can strike with greater energy at relatively short wavelengths to directly transfer patterns on hard materials (such as semiconductors, metals, or ceramics) without major forward- and back-scattering. Thus the feature size of the patterns is largely dictated by the beam size and the interaction of the beam with the target material. On the other hand, the electron or photon beam can mainly be applied for writing on soft materials (such as polymers or resists) and the corresponding feature sizes are determined by the proximity of the back-scattered electrons or wave diffraction limits.[1] Moreover, the lateral exposure in FIB technology is very low, thereby exposing the correct areas and writing very narrow lines in the substrate, which makes it more capable to directly fabricate nanostructures. Consequently, FIBs have become a popular fabrication tool adopted by the semiconductor industry, for mask repairing, device modification, integrated circuit (IC) debugging, and on-line inspection, as well as a powerful tool in making high-quality and high-precision nanostructures.[2–4]

The technology of using FIBs for nanofabrication is also called *direct writing*, which transfers patterns by direct impingement of a small spot of the FIB onto a substrate. Direct writing is a collection of several major approaches, including milling, implantation, ion-induced deposition, and ion-assisted etching, which respectively perform material removal from, property change on, material addition on, and material removal from the substrates with or without chemical assistance. The key to the FIB direct-write technology is its ability to operate a FIB with a proper beam size, current, and energy to remove or add a required amount of material with or without chemical reactions from a predefined location in a controllable manner. In this way, high-precision and complex three-dimensional (3D) nanostructures can be created.

Another major fabrication mode is called *projection printing*, which uses a 'collimated' beam of ions that passes through a stencil mask to form a pattern that is projected and printed onto the substrate using electromagnetic lens systems. The technology of ion projection printing, also known as ion projection lithography (IPL), originates from the semiconductor industry. It enables parallel production of a large number of devices and has been one of the major candidates for next-generation lithography (NGL) to complement the current optical lithographic technology (note that the latest developments and applications of IPL have been thoroughly reviewed recently[5]).

In this Review, FIB technology will be examined. Direct-writing techniques will be explored for their abilities

[*] Prof. A. A. Tseng
Department of Mechanical and Aerospace Engineering
Arizona State University, Tempe, Arizona 85287-6106 (USA)
Fax: (+1) 480-965-1384
E-mail: ampere.tseng@asu.edu

in fabricating nanostructures. The ion source and equipment for FIB are first examined; the principles and techniques of four FIB-related approaches: milling, implantation, ion-induced deposition, and ion-assisted etching, are then introduced and evaluated separately. The versatility and advancement of each approach will be assessed. The nanostructures resulting from different techniques will be presented to illustrate their feasibility and resolution. Finally, a summary of the current progress and the scope recommended for future developments are provided to conclude the study.

## 2. Ion Sources and Systems

Ions, usually atoms lacking one or more orbiting electrons, are particles with net electrical charges and can therefore be steered by electric or magnetic fields. Depending on the atomic species, the associated ion wavelength can be more than a million times shorter than that of visible light. In this section, both the sources and equipment systems used for FIB direct writing are evaluated.

### 2.1. Ion Sources

Liquid-metal ion sources (LMISs) are the most popular source for FIB. They are high-brightness ion sources and can produce a beam of heaver ions that can be focused onto fine spots on the order of 10 nm with adequate current densities for direct writing. Almost all metals that have relatively low melting temperatures and low reactivity can be used as the sources. The range of materials being used in FIB systems is also expanding to further increase the extent of their applications. The ion sources that are currently available include Al, As, Au, Be, Bi, Cs, Cu, Ga, Ge, Er, Fe, In, Li, Ni, Pb, Pd, Pr, Pt, U, and Zn.[4] Among these, Ga is the most popular ion species used in FIB for direct writing. In order to lower the melting point and to control the reactivity, alloy sources, such as PdAs, PdAsB, AuSi, and AuSiBe, are frequently used to deliver the dopants for semiconductors.[6]

Ampere A. Tseng is a Professor at Arizona State University. He received his PhD in mechanical engineering from the Georgia Institute of Technology in 1978, and has published more than 200 peer-reviewed articles, edited more than ten technical books, and is the holder of ten US patents. He was a recipient of the Superior Performance Award and ASU Faculty Award (1999–2000). He chaired the ASME Materials Division in 1991–92 and was elected as an ASME Fellow in 1995. He also chaired the NSF Workshop on Manufacturing MEMS (2000) and co-chaired the International Conference of Transport Phenomena in Processing (1992) and the USA–China Workshop on Advanced Machine Tool Research (1999).

A typical LMIS consists of a capillary tube with a needle through it, an extraction electrode, and a shield. The capillary acts as a reservoir that feeds liquid metal to the tip. The interaction of the strong electrostatic force generated by the extraction electrode and the surface tension causes the liquid-metal meniscus to form a sharply peaked cone, known as the Taylor cone. The application of the critical Taylor voltage on the liquid-metal cone extracts positively charged ions. The ions are condensed into focused parallel beams by the lens and ground electrodes, also called the upper or condenser lens.[4]

### 2.2. FIB Systems

The basic components of an FIB system consist of an ion source, ion optics, a substrate stage, and a vacuum chamber with auxiliary equipment. The frontispiece image of this Review schematically shows an FIB system with an LMIS. The ions are focused and collimated into parallel beams by the upper (condenser) lens. Then, the ion beam is passed through a mass separator and a drift tube. A mass separator is only necessary for high-energy systems equipped with liquid alloy ion sources. It is a setup to filter out unwanted ion species emitted from the alloy ion sources by allowing only the required ions with a fixed mass/charge ratio to pass through. Below the mass separator, there is a long collinear drift tube equipped with a stigmatic focusing lens for stigmatism and collimation, which eliminates the ions that are not directed vertically. The lower (objective) lens is located below the drift tube and helps to reduce the beam size and to improve focusing of the beam. Following the objective lens is an electrostatic beam deflector that controls the final trajectory or landing location of the ions on the substrate.

Many accessories, including the nozzle shown in the frontispiece, are equipped for FIB-assisted etching and induced deposition. Also, in processing insulated substrates, a nozzle type of equipment is needed to provide low-energy nonfocused electrons to compensate the charging on the substrate surface and to neutralize the substrate. Often, a multichannel plate (MCP) is located above the target. The MCP helps in recording the secondary electron emission and thereby, helps in imaging the substrate. All the components are usually placed in a low-pressure chamber evacuated to $10^{-7}$ Torr. This is done so that the mean free paths of the ions are increased and the strength of the beam is not reduced due to the interference of the particles in the chamber.[4,7]

## 3. Milling

Essentially, milling is a process combining physical sputtering, material redeposition, and amorphization (swelling). In this section, following a study of sputtering, the effects of redeposition and amorphization are discussed. The combined effects in milling are then illustrated and quantified by evaluating the milling yields in creating several basic

  

NANO MICRO small

nanostructures. An understanding of these milled structures and associated milling yields can lead to improving the dimensional controllability and enhancing the material removal efficiency for milling more complex nanostructures.

### 3.1. Sputtering

Sputtering is a major mechanism for material removal and its efficiency is normally represented by sputter yield, defined as the number of atoms ejected from the target surface per incident ion. A software package called SRIM (Stopping and Range of Ions in Matter) has been widely used for predicting the sputter yield for many different ions at a wide energy range. SRIM uses a Monte Carlo treatment of ion–atom collisions to calculate the stopping range of ions (10 eV to 2 GeV per atomic mass unit) into matter.[8,9] It can predict the distribution of ions and kinetic phenomena associated with the ion's energy loss, including target damage, phonon production, ionization, ion reflection, implantation, and sputtering.

In general, the sputter yield grows as the ion energy increases, but its rate of increase declines. In most cases, the sputter yield either levels off or decreases for ion energies higher than an energy where the implantation becomes dominant, which is frequently in the area of 100 keV as ions penetrate the substrate and are trapped in the crystal lattice. Also, increasing the incidence angle increases the sputter yield until the yield is maximized near 80°; then, it decreases very rapidly to zero as the incident angle approaches 90°. Roughly speaking, heavier ion sources or lower surface binding energies (or sublimation energies) of target materials can produce higher sputter yields. Also, a decrease in the target sublimation energy causes higher sputter yields due to the fact that sputtering is a phase-change process, in which an atom from a material in the solid phase is ejected into the gas phase.

Recently, to quantify the sputter yield and to gauge the reliability of SRIM, the author of this Review compared the SRIM predictions with more than ten sets of experimental data involving two different ions (Ar and Ga) impinging on two types of substrates (Au and Si).[4] SRIM predictions agree very well with the experimental data for the cases considered and the sputter yield is dependent not only on the substrate material, but also on many processing parameters including the ion energy, angle of incidence, and scanning procedures.

### 3.2. Redeposition and Amorphization (Swelling)

Normally, the sputtered atoms (neutral atoms and ions), which are ejected from the solid surface into the gas phase, are not at thermodynamic equilibrium. Consequently, they tend to condense back into the solid phase upon collision with any solid surface nearby and a portion of the ejected atoms may bump into the already sputtered surface and redeposit on it. For example, in channel milling, there is a certain possibility that the atoms ejected from the bottom of the milled channel will collide with the milled sidewalls and be redeposited. Redeposition can be greatly reduced if multiple passes instead of a single pass are used in milling with the same amount of ions.[4] With multiple passes, each successive pass removes redeposited material from the previous pass. In general, redeposition is affected not only by the scanning pattern of milling, but also by the milled geometry, the dynamics of the ejected atoms, and the sticking coefficient of the target material. Normally, redeposition reduces the milling rate and the aspect ratio of the milled structures. Redeposition also makes it difficult to accurately measure the degree of material removal and also hard to predict the final geometry because a certain portion of the sputtered atoms may be removed by the vacuum pumping system or redeposited outside the milling area.

If the energy or dose level of the incident ions is not high enough for sputtering, amorphization may occur in the bombarded area of a crystalline substrate and may induce the substrate to swell. For example, in the case of a crystallized Si substrate bombarded by Ga ions, the dose level that causes amorphization is on the order of $10^{15}$ ions $cm^{-2}$, while the effective sputtering dose should be at least two orders of magnitude higher than the amorphization dose.[10,11] In amorphization, the incident ions in most cases are buried in the target material and may also displace the target atoms from their lattice sites so that the displaced atoms are relocated to a nearby region. In the case of silicon, its density in the amorphous state is much lower than that of crystalline silicon, as reported by Custer et al.[12] Also, since the volume of swelling is much larger than the volume of the buried or implanted ions, swelling can be largely caused by density changes or amorphization, rather than exclusively by the buried or implanted ions. The magnitude of the swelling due to amorphization can be as high as tens of nanometers. Thus amorphization can diminish the dimensional accuracy of nanostructures and is an important consideration in nanofabrication. Understanding amorphization should be the first step to successfully minimizing or controlling it. Both milling and amorphization will be quantitatively estimated in later sections.

### 3.3. Nanoscale Holes and Arrays

Li et al.[13] have used a 30 keV $Ga^+$ FIB to mill an array pattern of nanoholes (dots) with a single pass on highly n-doped single-crystal Si(100) substrates. One of the dot-array profiles milled at 1 pA with a dwell time of 2 s for each dot using a beam full-width half-maximum (FWHM) diameter of 10 nm is shown in Figure 1. As shown, each hole (dot) has a V-shaped cross section and is approximately 20 nm in depth and 50 nm in diameter with a pronounced ring-shaped structure that surrounds the crater. In fact, the protruded ring structure is the swelling of the substrate due to amorphization and is the inherent shape obtained by single-pass FIB milling. Since most of the FIB roughly resembles a Gaussian ion distribution, the intensity at the fringe (tail) of the beam is much smaller than that at the core (center region). Thus it is not strong enough to sputter materials,

  

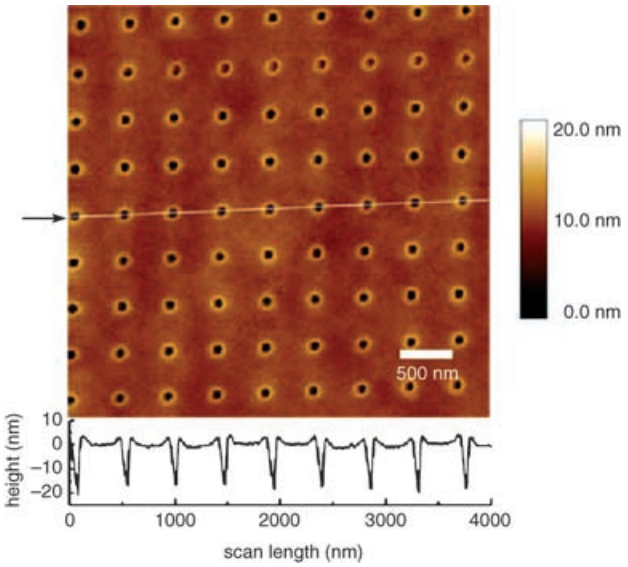


**Figure 1.** AFM image of hole (dot) array milled by a 30 keV $Ga^+$ FIB at 1 pA on a Si substrate (after Li et al.[13]).

but is sufficient enough to cause amorphization, which induces substrate swelling.[4] The ridge or protrusion height shown in Figure 1 is mainly a result of the swelling of the substrate and can be as high as ≈10 nm. Redeposition may add materials in the ridge, but the amount of material added should be much less than that added due to swelling (the gravity effect on redeposition is negligible here). The patterned Si substrate can be used as a master to replicate a polydimethylsiloxane (PDMS) stamp for nanoscale soft-imprint lithography applications.[14,15]

Milling of basic patterns, such as holes, has been directly applied for making many vital components used in industry. For example, Grabiec et al.[16] have successfully used a 30 keV $Ga^+$ FIB for milling (drilling) 30–100 nm diameter holes as the apertures in hollow pyramids used for scanning near-field optical microscopes, in which the aperture diameter has to be well below the optical wavelength. For these holes, the aspect ratios of the depth to the diameter cannot be made higher than five. The reproducibility and resulting optical quality based on other fabrication techniques are far inferior to that of FIB milling, as reported by the authors. Ohkouchi et al.[17] also used a 30 keV $Ga^+$ FIB for milling an aperture in the pyramidal tip of an atomic force microscope (AFM) probe, in which the drilled pyramidal tip was adopted as a nozzle for the deposition of an array of In nanodots on GaAs substrates with periods of 50 nm, and the AFM scanning mechanism was used to control the positions of these nanodot structures.

### 3.4. Nanoscale Channels

Tseng et al.[18] studied the single-pass milling of several nano- and microchannel patterns on a gold-coated substrate using a 90 keV $As^{2+}$ FIB with a beam FWHM diameter of 50 nm, a beam current ($I_p$) of 5 pA, a pixel spacing ($p_s$) of 14.5 nm, and a dwell time ($t_d$) varying from 5 to 50 ms. The AFM image in Figure 2a depicts the pattern milled with 5 ms dwell time and indicates ridges being formed along the channel banks (shoulders). Figure 2b shows that the corresponding cross-sectional profile is V-shaped and is characterized by four features: the ridge width (A), mouth width (B), channel depth (C), and ridge height (D). Figure 2c delineates the variations of the four features with respect to the dwell time, indicating that all of the features increase linearly with the dwell time in a double-logarithm plot. If the data is presented in a uniform scale, the corresponding rate of increase in the feature size gradually declines as the dwell time increases. This indicates that a large amount of sputtered material is being redeposited into the channel, since without redeposition the rate of increase of the milling depth and mouth width with the dwell time should be constant. Normally, the mouth width (B) and channel depth (C) are measures of material removal or milling rate, while the ridge width (A) and height (D) are used to characterize the swelling or amorphization effects. Based on an assumption that the sputtered particles are randomly ejected from the surface with an angular distribution statistically close to a cosine-squared function with a maximum normal to the sur-

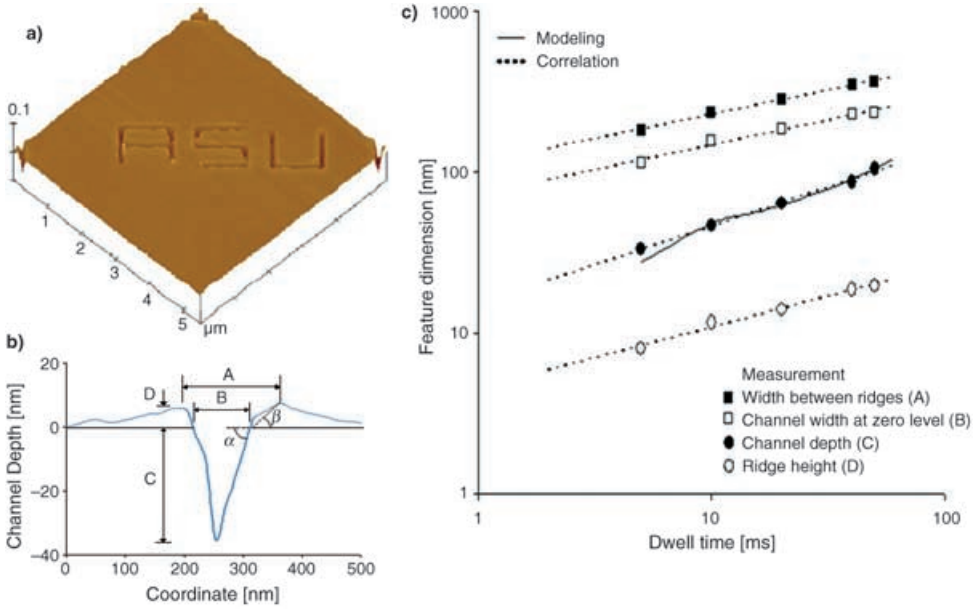


**Figure 2.** 'ASU' nanochannel pattern on a gold layer milled by a 90 keV $As^{2+}$ FIB: a) AFM image at a dwell time of 5 ms, b) channel cross section and feature definition, c) feature measurements for various dwell times.

face, a model has been developed to simulate channel milling by considering both the sputtering and redeposition effects; their predictions on the variation of the channel depth versus the dwell time agree very well with the measurements shown in Figure 2c.[19]

Frey et al.[10] and Li et al.[13] have used a 30 keV $Ga^+$ FIB to mill nanoscale channels with a single pass on Si substrates. They used different beam diameters at different beam currents and found that the channels milled by a single pass have a 'V'-shaped cross-section. The results further confirm that the V-shaped channel profile, similar to hole milling shown in Figure 1, is the inherent shape obtained by single-pass FIB milling. Also, the measurements shown in Figure 2c and reported by Li et al.[13] reveal that the mouth width of the V-shaped channel can be much larger than the beam diameter by almost one order of magnitude. This may suggest that at higher dwell times, the ion intensity outside of the core region of the FIB is sufficiently high enough to produce a sizeable amount of sputtering.

### 3.5. Milling Volume Yield

In the milling of nanostructures, the dimension accuracy has to be controlled within nanometer scales, and thus, the same precision should also be maintained at every milling step or "cut". Precise knowledge of the milling yield, especially the effects of ion doses on the milling yield, is essential to achieve sub-nanoscale precision. The volume yield ($Y_m$) is frequently used to gauge the milling yield and is defined as:

$$Y_m = dV_m/dQ \quad (1a)$$

where $V_m$ is the volume removed by milling and $Q$ is the ion charge. For simple 1D or 2D (hole, channel, or cavity) milling, the volume yield becomes:

$$Y_m = dM/dD \quad (1b)$$

where $M$ is the milling depth of the hole or channel (or any feature size in milling experiments) and $D$ is the ion dose, that is, the impinged ion charge per unit area.

It has been found that the relationship between the milling depth and the dwell time shown in Figure 2c can be converted to the relationship between the milling depth and the ion dose, since the beam diameter and current, as well as the pitch spacing, are known. The converted data can be plotted as a log–log curve (Figure 3). The data fits linearly in this log–log diagram following the relationship:

$$\log(M) = a + b\log(D) \quad (2)$$

where $a$ and $b$ are the correlation constants. If the relationship between the milling depth ($M$) and the ion dose ($D$) follows the relationship of Equation (2), the milling volume yield ($Y_m$) defined in Equation (1) can be found as:

$$Y_m = dM/dD = b(M/D) \quad (3)$$

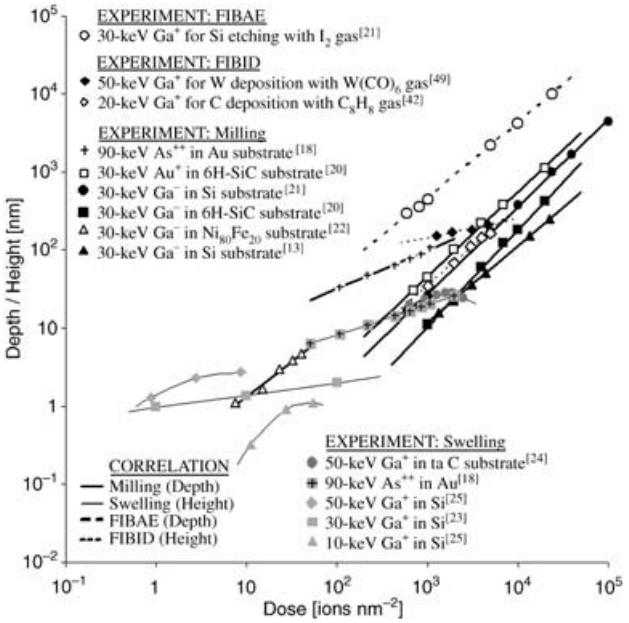


**Figure 3.** Relationship between feature size (depth by milling and etching or height by swelling and deposition) and ion doses for various ion species and materials.

The volume yield can be considered as the ultimate resolution in FIB milling, since it measures the amount of material removed by a single ion. In the later sections, the approach of the volume yield is also used to quantify the swelling rate ($Y_a$) as well as the FIB deposition rate ($Y_d$) and etching rate ($Y_e$).

Four more sets of experimental data for channel or cavity milling reported by Menzel et al.,[20] Park et al.,[21] Xiong et al.,[22] and Li et al.[13] are also selected for the correlation study. Menzel et al. studied cavity milling of crystalline silicon carbide (6H-SiC) using both $Ga^+$ and $Au^+$ FIB.[20] Park et al. investigated both FIB milling and assisted etching of Si substrates using 30 keV $Ga^+$ FIB to quantify the enhancement of material removal obtained by using $I_2$ gas.[21] Xiong et al. used a 30 keV $Ga^+$ FIB in milling $Ni_{80}Fe_{20}$ permalloy nanochannels.[22] Li et al. studied the nanochannel profiles at several dwell times (0.1, 1, 10, and 100 μs) and beam currents (1, 4, 11, and 70 pA).[13] The correlation results of these four data sets are depicted in Figure 3.

For further examinations, the numerical values of the correlation constants extracted from the data in Figure 3 are reported in Table 1. As shown in Figure 3, all milling data fit the log–log relationship very well and the corresponding coefficients of determination ($R^2$) reported in Table 1 for all data considered are higher than 0.98, in which the coefficient $R^2$ is a measure of the accuracy of correlation and always lies between 0 and 1. A value of zero occurs when the two variables are totally independent of each other, while it reaches unity when the two variables correlate perfectly, that is, there is no deviation from the curve. The volume yields ($Y_m$) extracted from the data shown in Figure 3 are plotted in Figure 4 in logarithmic scale. The volume yields vary in a relatively narrow range, from $10^{-2}$

  

**Table 1.** Correlation constants for volume yield prediction.

| FIB Conditions[a] | $a$[b] | $b$[b] | $c$[b] | $R^2$ | Refs. |
|---|---|---|---|---|---|
| MILLING | | | | | |
| 90 keV $As^{2+}$ in Au substrate | 0.5297 | 0.4862 | – | 0.996 | [4] |
| 30 keV $Au^+$ in 6H-SiC substrate | −1.5855 | 1.0815 | – | 0.999 | [20] |
| 30 keV $Ga^+$ in Si substrate | −1.9184 | 1.1183 | – | 0.999 | [21] |
| 30 keV $Ga^+$ in 6H-SiC substrate | −2.6769 | 1.2323 | – | 0.998 | [20] |
| 30 keV $Ga^+$ in Si substrate | −1.8461 | 0.9731 | – | 1 | [13] |
| 30 keV $Ga^+$ in $Ni_{80}Fe_{20}$ substrate | −0.7714 | 0.9001 | – | 0.984 | [22] |
| SWELLING | | | | | |
| 50 keV $Ga^+$ in ta-C substrate | −7.9870 | 5.8766 | −0.9161 | 0.911 | [24] |
| 90 keV $As^{2+}$ in Au substrate | 0.1505 | 0.3797 | – | 0.987 | [18] |
| 50 keV $Ga^+$ in Si substrate | 0.1568 | 0.6305 | −0.3603 | 1 | [25] |
| 30 keV $Ga^+$ in Si substrate | −0.0204 | 0.1594 | – | 1 | [23] |
| 10 keV $Ga^+$ in Si substrate | −3.6276 | 4.3500 | −1.2885 | 0.999 | [25] |
| FIBID | | | | | |
| 50 keV $Ga^+$ for W deposition with $W(CO)_6$ gas | 1.4487 | 0.2344 | – | 0.970 | [49] |
| 20 keV $Ga^+$ for C deposition with $C_8H_8$ gas | −1.4520 | 0.9977 | – | 0.994 | [42] |
| FIBAE | | | | | |
| 30 keV $Ga^+$ for Si etching with $I_2$ gas | −0.2452 | 0.9679 | – | 1 | [21] |

[a] 6H-SiC = crystalline silicon carbide ; ta-C = diamond-like carbon. [b] Units: $a$ [nm], $b$ [$nm^3\,ion^{-1}$], $c$ [$nm^5\,ion^{-2}$].

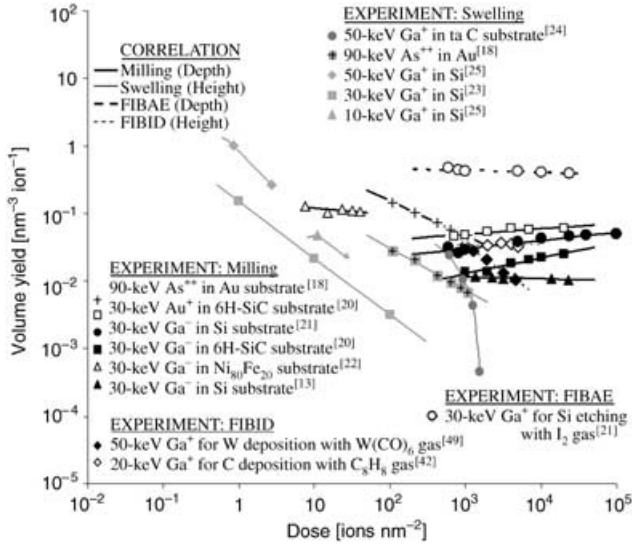


**Figure 4.** Relationship between volume yield and ion doses for various ion species and materials.

to $2\times10^{-1}\,nm^3\,ion^{-1}$. The yields decrease linearly with the ion dose, which implies that the effects of redeposition increase as the milling depth or ion dose increases.

### 3.6. Swelling Volume Yields

In addition to the amorphization data (ridge height and width) shown in Figure 2,[18] the effect of ion dose on swelling or amorphization has been studied by Huey and Langford using $Ga^+$ FIBs to mill Si substrates.[23] Their results fit the log–log relationship, similar to Equation (2), very well:

$$\log(A) = a + b\log(D) \quad (4)$$

where $A$ is the amorphization size or swelling height, and $a$ and $b$ are the correlation constants, similar to those in Equation (2). However, based on the studies by Stanishevsky[24] using a 50 keV $Ga^+$ FIB to mill a diamond-like carbon (ta-C) substrate and by Lugstein et al.[25] using $Ga^+$ FIBs to mill Si substrates, the swelling results indicate that the amorphization size (swelling height) increases with the ion dose, but after reaching a maximum, it decreases as the ion dose increases. Their experimental data correlate well with the following relationship:

$$\log(A) = a + b\log(D) + c(\log(D))^2 \quad (5)$$

where $a$, $b$, and $c$ are the correlation constants. If constant $c$ is zero, Equation (5) is reduced to Equation (4). All the amorphization results are also summarized in Figure 3 and indicate that the dose level causing amorphization is in the range of $10^0$ to $10^2$ ions $nm^{-2}$ for the Si substrate, and $5\times10^2$ to $10^3$ ions $nm^{-2}$ for ta-C. Figure 3 also shows that the magnitude of the swelling sizes in ta-C is one order greater than that of Si using a 50 keV $Ga^+$ FIB. Although Huey and Langford[23] and Tseng et al.[18] reported that the swelling sizes increase monotonically with the ion dose as shown in Figure 3, it is expected that the amorphization sizes would decrease at higher doses for these cases. To verify this, a further study is encouraged.

Since the swelling size follows both linear and nonlinear relationship, the more general nonlinear formulation, Equation (5), is used for quantification. The corresponding swelling volume yield for amorphization ($Y_a$) can be found as

$$Y_a = dA/dD = [b + 2c\log(D)](A/D) \quad (6)$$

If the logarithmic relationship of amorphization ($A$) is really linear, constant $c$ becomes zero and Equation (6) is identical to Equation (3). Again, the volume yields extracted from the data shown in Figure 3 are plotted in Figure 4

  

NANO MICRO small

on a logarithmic scale. As shown in Figure 4, the volume yield based on the data by Huey and Langford[21] and Tseng et al.[18] linearly decreases with the ion dose, but at a steeper rate of decline. The magnitude of their swelling yields can be as large as their milling counterparts.

If amorphization behaves nonlinearly, that is, the swelling in some dose ranges decreases with increased dose, the constant $c$ in Equation (6) is not zero, and the corresponding volume yields can be negative. If this is the case, only positive volume yields are plotted in Figure 4, since the log–log scale in Figure 4 can not accommodate the negative values. As a result, in the cases of Stanishevsky[24] and Lugstein et al.,[25] only the initial volume yields are depicted in Figure 4, because in the higher dose range the swelling sizes of their amorphization results diminish as the dose increases and result in negative volume yields. These initial swelling volume yields vary in a relatively wide range, from $5\times10^{-4}$ to $1\,nm^3\,ion^{-1}$. Also, the initial swelling yield can be one order of magnitude larger than that of milling. This is somewhat interesting because one would expect that the swelling yield should be smaller than its milling counterpart. However, the results shown in Figure 4 are consistent with our earlier discussion. In the case of silicon, the density in the amorphous state is much lower than that of crystalline silicon, and thus swelling should be largely contributed by the density changes or the amorphization, rather than exclusively by the buried or implanted ions. The magnitude of the swelling due to amorphization can be as high as tens of nanometers.

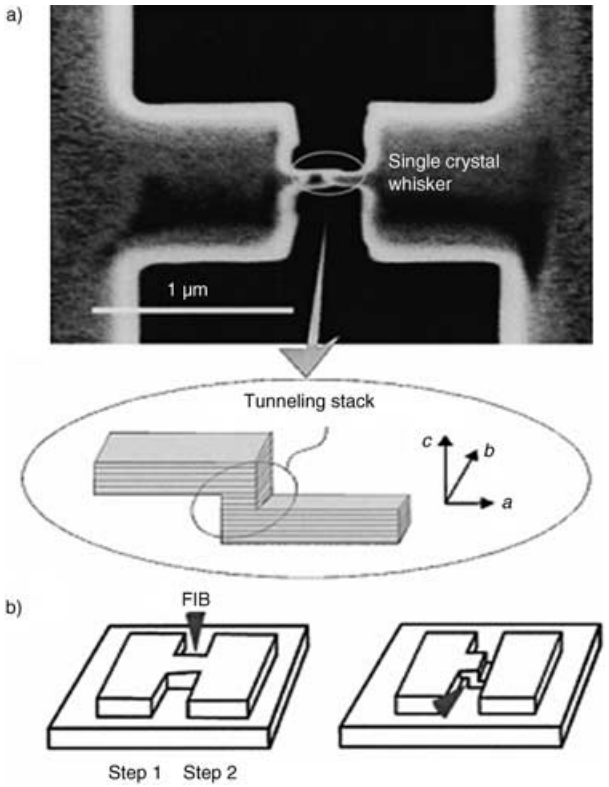


**Figure 5.** Stacked nanostructure: a) SIM image of an intrinsic Josephson junction with a 0.01 $\mu m^2$ ($\approx$100 nm × 100 nm) tunneling stack, b) FIB fabrication steps (after Kim et al.[26]).

### 3.7. Layered Nanostructures

Kim et al.[26] used a 30 keV $Ga^+$ FIB to mill an intrinsic Josephson junction (IJJ) structure used as the basic element for quantum computation. The IJJ is a Z-shaped stacked structure prepared from $Bi_2Sr_2CuO_{6+\delta}$ (Bi-2201) single-crystal whiskers. As shown in Figure 5a, the intrinsic Josephson junction has a 0.01 $\mu m^2$ ($\approx$100 nm × 100 nm) tunneling stack area. The 3D tunneling stacks were patterned on a special rotation stage. The steps of the FIB milling process are shown in Figure 5b. The width of the whisker was first milled from the perpendicular direction ($c$ direction in the figure) to a size dictated by the junction dimensions. Then, by tilting the sample stage up to 90°, two grooves of the bridge were milled completely from the lateral sides ($b$ direction) in order to create the required junction shape. This technique, FIB in concert with a rotation stage, can fabricate nanoscale stacks from thin films or single crystals.

Molecular electronics, in which a single molecule is used as an element, frequently require electrodes to interface nanometer-sized molecules to macroscopic electronic circuits. The gaps of these metallic electrodes are required to be comparable in size to single molecules and this type of electrode is also known as a "nanogap electrode". However, fabricating such electrodes presents difficulties because the size of single molecules, on the order of less than 10 nm, is smaller than the resolution limits of the popular electron-beam lithography (EBL; $\approx$20 nm). Nagase et al. used a 30 keV $Ga^+$ FIB to directly pattern a 44-nm-thick Ti mask for making 70-nm-thick Au electrodes with a gap of 5 nm on a $SiO_2$ substrate.[27] The gap pattern of the Si mask, which is milled by an FIB with a FWHM diameter of 12 nm, is 12 nm wide, the same as the beam diameter. The electrode mask pattern is then transferred to the underlying Au layer to form the electrodes by $Ar^+$ reactive-ion etching (RIE) and the remaining Ti mask is subsequently removed by hot wet-etching using a $H_2SO_4$:$H_2O$ solution.

## 4. Implantation

The FIB system not only has capabilities of performing subtractive (milling and etching) processes, but it can also perform additive (implantation and deposition) processes. In this section, the implantation ability of FIB will be explored by showing the specific procedures used in creating different nanostructures.

### 4.1. Nanocantilevers and Nanocups

A combination of FIB implantation (FIBI) and wet etching has been used to fabricate a nanoscale quad-cantilever on a Si(100) substrate with 10 Ω n-type background doping. As shown in Figure 6a and b, the quad-cantilever is

  

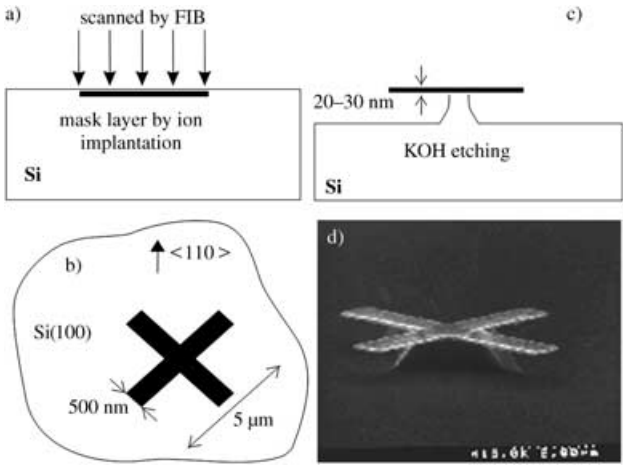


**Figure 6.** Nanocantilevers on a Si substrate and processing steps: a) implantation or modification by FIB scanning (cross section), b) top view of a FIB-scanned surface with a quad-cantilever layout, c) KOH etching for a non-implanted substrate (cross section), d) SEM image of fabricated quad-cantilevers, which are 30 nm thick, 500 nm wide, and 5 μm long (courtesy of J. Brugger of the Swiss Federal Institute of Technology).

first patterned by ion implantation using a 30 keV $Ga^+$ FIB at 100 pA in the Si substrate at a sufficiently high dose, namely, higher than 10 ions $nm^{-2}$. At this level of dose concentrations, that is, higher than 10 $Ga^+$ ions $nm^{-2}$ in silicon, the etch rate of certain etchants, including KOH, can be dramatically reduced and the doped silicon can be used as an etch stop or a mask in IC fabrication.[28] The thickness of the cantilever structure is dictated by the penetration depth (or the range) of the implanted ions, which can be controlled by the incident energy of the ions. Therefore, selective etching is accomplished as the substrate is dipped into a 40% KOH solution at 60 °C, in which the silicon layer with no implantation is etched away at a rate of 4 nm $s^{-1}$, while the implanted region is relatively unaffected (Figure 6c). A 3D quad-cantilever that is 20–30 nm thick, 500 nm wide, and 5 mm long, is formed (see SEM image in Figure 6d).

This technique, which uses ion-implanted layers as the etching mask for subsequent dry or wet etching, is expected to be one of the major fabrication techniques for nanostructures. Brugger et al. have used a similar approach to etch several nanoscale freestanding structures, including a 30-nm-thick cup and a 30-nm-thick U-shaped cantilever.[29] Earlier, Xu and Steckl used a 30 keV $Ga^+$ FIB to implant n-type Si with a dose level of 10 ions $nm^{-2}$ as the etch mask for subsequent KOH etching to make microscale cantilevers.[30]

### 4.2. Nanogroove Arrays

Utilizing a similar procedure as above, namely, implantation combined with etching, Hiramoto et al. fabricated an array of grooves on epitaxial AlGaAs layers.[31] Implantation was performed by line scanning of a $Si^+$ FIB with a FWHM diameter of 100 nm at 200 keV. They found that the cross sections of the doped area could be varied from U-shaped to round by reducing scanning speeds or increasing the doses. Figure 7 shows round-shaped grooves that are wider in the interior and narrower near the surface. Using a

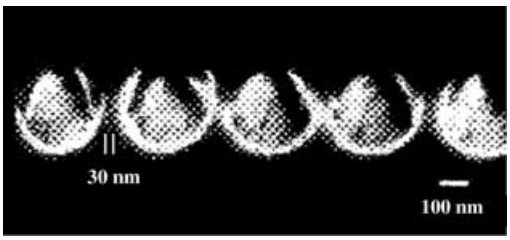


**Figure 7.** SEM image of a groove array fabricated by Si-FIB implantation on AlGaAs substrates (after Hiramoto et al.[31]).

hot HCl etchant at 70 °C, the grooves are formed by selectively etching a highly doped region that is implanted at a scanning speed of 0.1 mm $s^{-1}$ and a line dose of $10^3$ ions $nm^{-1}$. The round grooves are about 350 nm in diameter and the distances between the etched grooves are about 30 nm. Since the groove diameter is much larger than the beam diameter (100 nm), the implanted ions are spread into the substrate and the grooves can be implanted very close at a distance much less than the beam diameter. A similar technique was also applied to make very small GaAs conducting wires ranging from 20 to 100 nm in diameter.[31]

### 4.3. Nanoscale Lines and Dots

Bai et al. used a 40 keV $Si^{2+}$ FIB to implant fine patterns on an n-type silicon-film-on-sapphire (SOS) substrate.[32] If the ion dose is high enough, the implanted or irradiated regions become amorphous and some solutions can etch the non-irradiated area without removing the implanted region. As shown in the SEM image in Figure 8a, a line-pad structure, which is fabricated by FIB implantation and subsequent etching treatment using an aqueous solution of tetramethylammonium hydroxide (TMAH), has a line width of 100 nm on the top near the 550-nm-thick pad. The FWHM diameter of the FIB is 100 nm with a dose of 20 ions $nm^{-2}$. The final shape can be further optimized by ad-

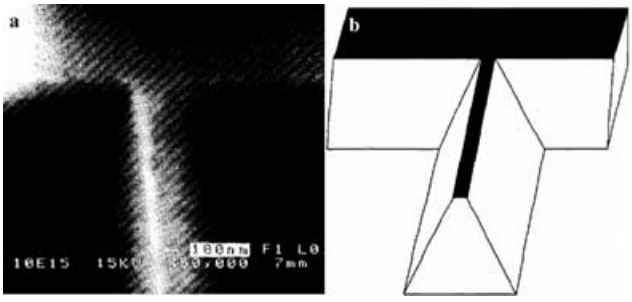


**Figure 8.** Line-pad Si structure formed by TMAH etching after patterning by $Si^{2+}$ implantation: a) SEM image, b) schematic of the line-pad (after Bai et al.[32]).

small NANO MICRO

justing the FIB irradiation and etching conditions. The technique, which uses ions to weaken the material to act as a negative etching mask, is the opposite of the technique shown in Figure 6, in which the implanted layer is used as a positive etching mask.

Similarly, Prevel et al. used a 35 keV $Ga^+$ FIB with a beam diameter of 5 nm at a current of 6 pA to irradiate a dot-array pattern on a graphite substrate, in which the irradiated dots act as nucleation sites for deposited Au clusters using laser evaporation sources.[33] During the deposition, the vaporized Au is at a highly non-equilibrium state and is trapped directly upon contact by the irradiated surface to form Au clusters. The size, shape, and pattern of the clusters are highly dependent on the shape of the dose level of the FIB irradiation. Gold nanodot clusters with diameters less than 100 nm at a periodicity of 300 nm have also been demonstrated by Prevel et al.[33] The demonstration indicates that this technique has great potential to organize nanostructures on patterned surfaces with ultrahigh resolution at high speeds.

### 4.4. Polymeric Nanolines

FIB implantation has been used for irradiating polymeric resist materials to increase their resistance to subsequent physical etching. Arshak et al. used a 30 keV $Ga^+$ FIB with $1.17 \times 10^{-2}$ C cm$^{-2}$ doses to make implanted patterns in Shipley SPR660 positive photoresist layers, which can form $Ga_2O_3$ to be used in $O_2$ RIE.[34] This process, also known as "graphitization", can harden the photoresist to be conveniently used as an etching mask for $O_2$ dry etching. As shown in the FIB image in Figure 9, two 100 nm negative resist

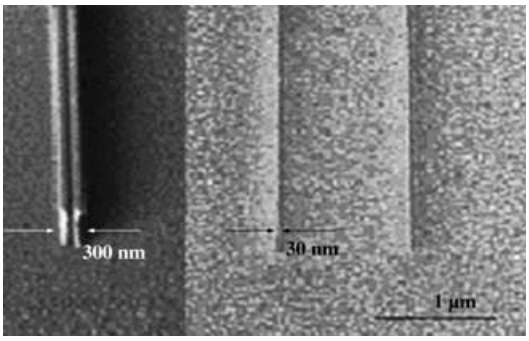


**Figure 9.** FIB images of double 100 nm (left) and 30 nm (right) lines patterned by FIB implantation in SPR660 photoresist after $O_2$ RIE (courtesy of Khalil Arshak of the University of Limerick, Ireland).

lines with a 100 nm space (left) and two 30 nm resist lines (right) were patterned after RIE in the SPR660 resist layer. This demonstrates that anisotropic patterns can be achieved by graphitization and can be directly incorporated into standard photolithographic processes.

### 4.5. Changing Properties

Ion implantation has also been used to change the electrical, optical, magnetic, and etching properties of different materials for making nanodevices. In the case of changing electrical properties, Sumita et al. fabricated a charge-density-wave (CDW) device having a 40 nm thickness and 100 nm width and found that the device shows collective sliding and negative resistance above a threshold electric field in the low-temperature region.[35] This suggests that quantum tunneling phenomena occur in the fabricated CDW, which can only result from a condition that the structure is a true 1D conductor or is narrow enough to cause collective sliding of electrons without interference. This 1D structure is patterned by two types of ion implantation in a $K_{0.3}MoO_3$ conducting substrate. Ion implantation with sufficient doses renders the substrate material nonconducting, and the implanted regions can act as insulators to separate the conducting regions and prevent electronic interference. A 4.5 keV $H^+$ FIB is used to irradiate the substrate to make a region 40 nm underneath the surface that has sufficient dose to annihilate the CDW, in order to profile the thickness of the 1D conductor. A 60 keV $Si^{2+}$ FIB is then applied to partition the width of the conductor. In order to change optical and magnetic properties, Kalbitzer has used FIB implantation on different semiconducting materials to make optical nanostructures,[36] while Khizroev and Litvinov have studied the influence of implantation by a $Ga^+$ FIB on magnetic materials for making nanoscale magnetic devices.[37]

In many cases, implantation of insulating materials can significantly increase their etch rates and can be used for etching stop or masks. For example, as reported by Ryssel and Ruge,[38] with appropriate levels of doses and etchants, the etch rate of $SiO_2$ substrates implanted by Ar, P, and B ions can be increased at least five times as compared with that of non-damaged regions, while the etch rate of $Si_2N_4$ can be elevated 10 times by implanting Sb ions. Both $SiO_2$ and $Si_2N_4$ are important masking materials in semiconductor processing. Heavily B-ion-doped Si has also been frequently adopted as an etch stop or mask for different etching processes for nanoelectromechanical systems (NEMS) devices.[39]

With regard to equipment development, Shinada et al. have improved FIB optics for single-ion implantation.[40] This high-precision implantation instrument can perform one-by-one doping of impurity ions into nanoscale semiconductor devices for various applications. In general, the precision in ion implantation is dictated mainly by controlling the level of irradiation damage and the duration and position of FIB. A structure of 20 nm scale is achievable at present and that of a 5 nm scale may be realized soon by improving the implantation precision.

## 5. FIB-Induced Deposition

FIB can be used as a deposition tool for fabricating nanostructures. FIB-induced deposition (FIBID) uses ion energy to initiate and localize chemical vapor deposition

  

(CVD) in a specific location by a direct-writing technique, also known as FIBCVD. The FIB system should be equipped with a gas nozzle to allow the injection of a variety of organometallic precursor gases on the target surface in the vacuum chamber (shown in the frontispiece). The high-energy ion beam can decompose the organometallic molecules adsorbed onto the surface of the substrate. This leads to the release of metal atoms, which are incorporated at the surface. Meanwhile, the remaining species resulting from the decomposition reaction are generally volatile and can be eventually removed from the vacuum chamber with the pumping apparatus.

### 5.1. Precursor Gases

Many types of precursor gases have been used in FIBID for making of a variety of metallic and ceramic structures. For example, the precursor gases $WF_6$ (or $W(CO)_6$), $C_7H_7F_6O_2Au$, $(CH_3)_3NAlH_3$, $C_9H_{16}Pt$, and TMOS + $O_2$ (TMOS = tetramethyloxysilane) have been used to produce W, Au, Al, Pt, and $SiO_2$, respectively.[3] The gas nozzle is usually controlled at a height of 0.1 to 1 mm above the target surface at an angle of 30–60°, with the precursor gas being evaporated from a heated container. Some other gases can also interact with the FIB for removing a wide range of materials. This process is also known as "FIB-assisted etching", which will be discussed later.

### 5.2. 3D Deposition and Structures

The key for making 3D nanostructures by FIBID is its ability to deposit overhanging features that extend beyond the already-deposited structure underneath. The frontispiece shows a schematic diagram of the procedure used by many investigators for fabricating 3D overhung structures.[7,41] As shown, deposition proceeds layer by layer. In each scan or layer, the new deposition extends a bit more over the previously deposited layer. Normally, the size of the extension or overhang in each layer should not be larger than the layer thickness. The moving speeds of FIB in the $x$ and $y$ directions are controlled by the beam deflectors, while growth in the height ($z$) direction is determined by the deposition rate. This implies that the height of the structure is proportional to the irradiation time when the deposition rate is constant. Normally, the deposited structures can contain many types of impurities, including elements of the ion species, elements or impurities from the precursor gases and substrates, and contamination during deposition. As a result, their mechanical, optical, electrical, or magnetic properties can be significantly different from the corresponding properties of the pure material intended to be deposited.[42–46]

Matsui et al. fabricated several nanostructures using a 30 keV $Ga^+$ FIB having a 7 nm beam diameter with an aromatic hydrocarbon (AH) precursor gas for creating diamond-like carbon (DLC) nanostructures.[41] Figure 10a shows a scanning ion microscopy (SIM) image of microbellows with a thickness of 100 nm, a pitch of 800 nm, an external diameter of 2.75 μm, and a height of 6.1 μm. Normally, an SIM image looks more stereoscopic than an SEM image. The total exposure time was 300 s at a beam current of 16 pA and a dwell time of 200 ns. The vacuum chamber pressure is $2\times10^{-5}$ Pa, and after introducing the gas it is $5\times10^{-5}$ Pa. Figure 10b shows another nanostructure, a microcoil structure having a wire diameter of 80 nm with a 600 nm coil diameter and a 700 nm coil pitch. The microcoil was made with a dwell time of 0.11 s with a total exposure time of 40 s at a beam current 0.4 pA. By changing the FIB scanning speed or the deposition rate, the desired pattern with different coil pitches can be fabricated.

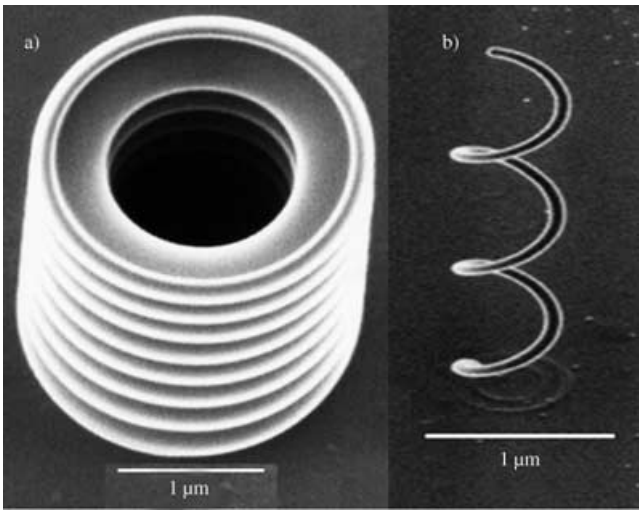


**Figure 10.** SIM images of nanostructures prepared by FIBID: a) microbellows with a 100 nm thickness, 800 nm pitch, 2.75 μm external diameter, and 6.1 μm height, b) microcoil with a 600 nm coil diameter, 700 nm coil pitch, and 80 nm wire diameter (courtesy of Shinji Matsui of the Himeji Institute of Technology).

Using a similar FIBID technique, a number of free-space-wiring (FSW) nanostructures have been fabricated by Morita et al. using phenanthrene (a polycyclic aromatic hydrocarbon) as the precursor gas.[45] Figure 11 shows SIM images of two nanostructures: a bridge and a parallel-resist-

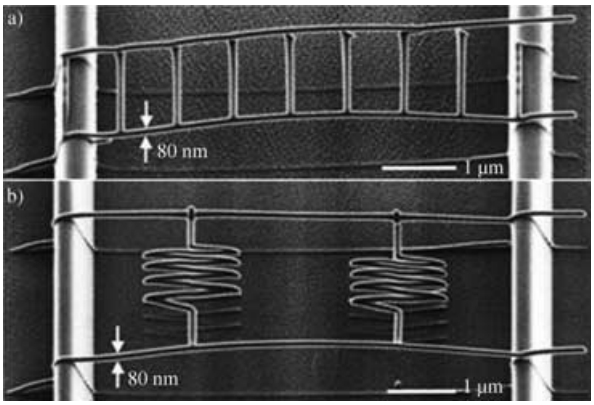


**Figure 11.** SIM images of DLC nanostructures prepared by FIBID: a) free-space-wiring with a bridge shape, b) free-space-wiring with parallel resistances (after Morita et al.[45]).

  

NANO MICRO small

ance component, where the growth time was 1.8 min for the former and 2.8 min for the latter. Both structures have a wiring diameter of 80 nm and are made of amorphous carbon (DLC) containing a Ga core, as verified by transmission-electron microscopy (TEM) and energy-dispersive X-ray (EDX) spectroscopy. In fabricating these FSW structures, the optimum beam scanning speed is 190 nm $s^{-1}$ at a beam current of 0.3–2.7 pA. If the scanning speed is faster than the optimum scanning speed, a FSW nanostructure fails. On the other hand, if the scanning speed is slower, a FSW grows with a slanted structure. It seems that appropriate control of the scanning speed is essential to make FSW structures. Because of the relatively large Young's modulus of the deposited DLC (over 600 GPa), Watanabe et al. have used a similar FIBID approach to making solid DLC nanostructures as the mold for hard imprinting applications.[47]

### 5.3. Device and IC Applications

Lin et al. used a Pt-based organometallic precursor to deposit a Pt nanostructure to serve as a nanointerconnect (NI) to structures such as carbon nanotubes and single molecules.[48] As shown in Figure 12, the Pt interconnect is deposited onto an insulating $SiO_2$ substrate with a cross section of 50 nm by 60 nm to bridge two terminal contact-structures made of a Ti/Au bilayer by photolithography. The same authors also studied the electromagnetic properties of the NI and revealed a small residual-resistivity ratio, and a Debye temperature that differs significantly from that of pure Pt, which is indicative of the disordered nature of the nanowires. Their magnetoresistance shows evidence for weak antilocalization at temperatures below 10 K with a phase-breaking length of ≈100 nm, and a temperature dependence suggestive of quasi-1D interference.

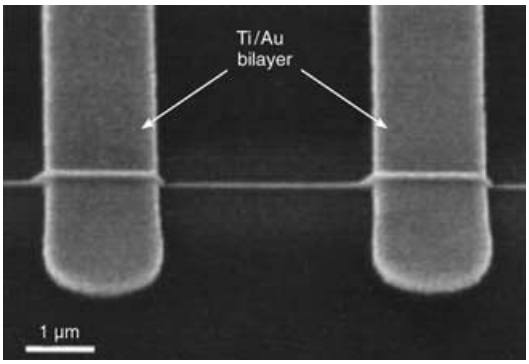


**Figure 12.** SEM image of a Pt nanointerconnect (≈50 nm × 60 nm cross section) constructed by FIBID, taken at a glancing angle of 45° (courtesy of J.-F. Lin, Arizona State University).

In the semiconductor industry, FIBID has been frequently used in IC editing or repairing, where flawed prototype designs are repaired by rerouting interconnects through FIB-deposited metal lines and insulating layers. FIBID has also been used in photolithographic mask repairing to add missing adsorber material. Furthermore, in cooperation with FIB milling, FIBID could become a useful tool in IC design by allowing circuitry modifications to be performed at the prototype stage. It should be noted that because organometallic compounds are used for metal deposition, the FIB deposits contain rather large amounts of carbon and the resistivity of these deposits is generally about one to two orders of magnitude higher than those of the pure metal. For most practical applications, this is not critical because the connections are rather short and the resistance can be adjusted by increasing the film thickness.[3]

Theoretically, as indicated in Figures 10 and 11, very tall nanostructures (aspect ratio larger than 100) with various mechanical strengths can be deposited. These types of high-aspect-ratio structures are quite unique and can be used for many industrial applications. Further efforts to reveal more unique applications for the nanostructures using FIBID are encouraged. Also, for the sake of comparison, the data of the height of the deposited structures at various ion doses reported by Harriott and Vasile,[42] and Langfischer et al.,[49] are plotted in Figure 3, while the corresponding volume yields are plotted in Figure 4. As shown, the volume yield is on the same order of magnitude as compared to milling, that is, FIBID is as efficient as FIB milling, in spite of the fact that a portion of the material deposited by FIBID is concurrently removed by sputtering.

## 6. FIB-Assisted Etching

In focused ion-beam-assisted etching (FIBAE), also known as chemical-assisted or gas-assisted ion etching, an ion beam is used to initiate a chemical reaction between the substrate surface and gas molecules absorbed on the substrate to enhance the material removal rate. By injecting a reactive gas precursor into the milling process, the material removal mechanism can be changed and the associated milled shape can be altered. To have better dimensional control, the spontaneous reaction between the precursor gas and the substrate needs to be avoided or minimized. The equipment setup for FIBAE is similar to that for deposition (shown in the frontispiece), but the precursor gas is different.

### 6.1. Precursor Gases

While ion milling can be used to remove almost all kinds of solid materials, FIBAE can only be applied to certain substrates since a precursor gas must exist to form volatile products with the substrate. Frequently used precursor gases in FIBAE include $Br_2$, $Cl_2$, $I_2$, and $XeF_2$ for etching certain metals and insulators, and water vapor is generally used for the etching of carbon-based materials. Also, mixtures have been developed for FIBAE, such as $Cl_2/NH_3$ for copper.[49] For some important materials, including Pt, Au, and most metal oxide compounds used in superconductors or ferroelectrics, effective etch chemicals are not yet available.

  

### 6.2. Challenges in Nanoscale Etching

The major advantages of FIBAE over FIB milling are higher material removal rates, lower redeposition on sidewalls, and reduced implantation damage. For higher material removal rates, as indicated in Figure 3 and 4 based on the data reported by Park et al.,[21] the volume yield increases by more than tenfold for making cavities in Si substrates using a 30 keV $Ga^+$ FIB with $I_2$ gas, as compared to that of FIB milling without the gas. However, in nanofabrication, the corresponding accuracy or resolution should be controlled within nanometers. The easiest way to achieve this is to 'minimize' the material removal rate at the sub-nanoscale level in a controllable manner. Since FIBAE has relatively high etching rates, too high to be used for removing materials in nanoscale amounts, it has seldom been used in nanofabrication.

In fact, the smallest feature sizes for the structures made by FIBAE have been found in the 200–300 nm range, which include an egg-crate pattern etched on a Cu layer using a Ga FIB with $W(CO)_6$ gas,[51] and parallel trenches on a diamond substrate by Ga ions using $XeF_2$ gas.[52] For a structure smaller than this range, the irregularities induced from etching, including pits, ripples, ridges, and roughness, which can be much larger than 10 nm even in the best controlled conditions, can overwhelm the intended shape or result in an unacceptable inaccuracy.[52–53] As an illustration, the SIM images in Figure 13 show a comparison of two crystalline diamond structures, respectively made by a 50 keV $Ga^+$ FIB with and without $XeF_2$ gas assistance, as reported by Stanishevsky.[54] Since an ion dose that is two times higher is required to compensate for the enhancement with $XeF_2$ gas in order to make identical patterns for comparison, the dose used in milling without gas is 10 nC μm$^{-2}$, compared with 5 nC μm$^{-2}$ for FIBAE. The initial lateral size of the mesas inside the patterns preset to 2×2 μm for both cases. Figure 13a shows that the top of the mesas milled without gas are changed by less than 5%, while the mesas made by FIBAE are reduced by about 50% from 2×2 μm to 1×1 μm at the top (Figure 13b).

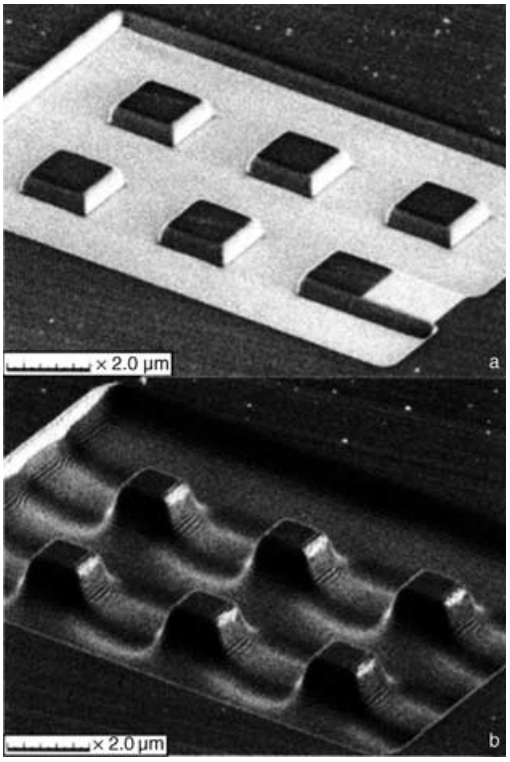


**Figure 13.** SIM images of two crystalline diamond structures using 50 keV $Ga^+$ FIB: a) a pattern milled without gas at an ion dose of 10 nC μm$^{-2}$, b) the same pattern prepared with $XeF_2$ gas assistance at an ion dose of 5 nC μm$^{-2}$. The initial lateral size of mesas inside the patterns was preset to 2 × 2 μm (after Stanishevsky[54]).

To claim the legitimacy or ability of nanofabrication, the feature sizes of the irregularities have to be controlled below a value much smaller than 10 nm. As indicated in the illustrations shown in Figure 13, the final shape of the pattern by FIBAE is quite different from that of the pattern milled without gas and the uncontrollable dimension deviation in FIBAE is indeed at the micrometer level. Consequently, in the remainder of this section, only the general characteristics of FIBAE are summarized and no nanostructures fabricated by FIBAE are reported.

### 6.3. Enhancement of Volume Yield

A great many investigators have studied the enhancement of material removal at various conditions by FIBID. Table 2 summarizes 26 data sets of the enhancement factor with the sources cited in the table. Here, the enhancement factor is the ratio of the material removal rate with gas-assistance to that of without gases. The factor can also be defined as the ratio of the gas-assisted milling yield to the sputter yield.[6] In fact, the differences in estimation of the enhancement factor from these two definitions are not significant.[54] The large variations reported by different authors are a result of the fact that, in contrast to physical sputtering, the yield for gas-assisted etching strongly depends on the experimental conditions, such as dwell and refresh time, current density, and gas pressure. Because the enhanced etch rate translated into a lower ion dose needed for material removal, adverse effects of ion milling, such as damage and implantation to underlying structures, are also greatly reduced. In general, reaction yield, that is, the number of atoms etched per incident ion, decreases as the dwell time increases until a steady state is attained. On the other hand, the reaction yield increases with the refresh time until a plateau is reached. As a result, the refresh time has to be long enough to obtain an initially fully saturated surface with the precursor etchant. The dwell time in FIBAE is the amount of time that the beam remains at the same location or pixel. The refresh time is the time between successive exposures of the same location and the time available to the gas molecules to be absorbed at the surfaces.

NANO MICRO small

**Table 2.** FIBAE enhancement for various materials and gases.

| Substrate | Ion (energy) | Gas flux (pressure) | Enhancement | Refs. |
|---|---|---|---|---|
| Al | Ga (30 keV) | $Cl_2$ (1.5 μTorr) | 3.0 | [56] |
| Al | Ga (25 keV) | $H_2O$ (70 mTorr) | 0.2 | [58] |
| Au | Ga (30 keV) | $Cl_2$ (1.5 μTorr) | $<2.0$ | [56] |
| Cu | Ga (50 keV) | $Cl_2$ (100 mTorr) | 2.0 | [50] |
| Diamond | Ga (50 keV) | $XeF_2$ (3.2 μTorr) | 3–7 | [54] |
| Diamond | Ga (50 keV) | $H_2O$ (3.2 μTorr) | 6–12 | [54] |
| Diamond | Ga (30 keV) | $XeF_2$ (3.0 Torr) | 6.0 | [52] |
| Diamond | Ga (25 keV) | $H_2O$ (70 mTorr) | 10 | [58] |
| Diamond | Ga (20 keV) | $H_2O$ (40 nTorr) | 2.0 | [53] |
| GaAs | Ga (30 keV) | $Cl_2$ (1.5 mTorr) | 10 | [56] |
| GaN | Ga (30 keV) | $XeF_2$ (3.2 μTorr) | 2.0 | [59] |
| GaN | Ga (30 keV) | $I_2$ (3.2 μTorr) | 10 | [59] |
| InP | Ga (35 keV) | $Cl_2$ (1.3 mTorr) | 20–30 | [60] |
| InP | Ga (30 keV) | $Cl_2$ (1.5 μtorr) | 4.2 | [56] |
| InP | Ga (30 keV) | $I_2$ (800 mTorr) | 11–13 | [61] |
| PMMA[a] | Ga (30 keV) | $Cl_2$ (1.5 μTorr) | 1.6 | [56] |
| PMMA | Ga (25 keV) | $H_2O$ (70 mTorr) | 20 | [58] |
| Si | Ga (65 keV) | $Cl_2$ (4 mTorr) | 20 | [60] |
| Si | Ga (30 keV) | $Cl_2$ (1.5 μTorr) | 11.8 | [56] |
| Si | Ga (25 keV) | $H_2O$ (70 mTorr) | 0.3 | [58] |
| $SiO_2$ | Ar (50 keV) | $XeF_2$ (20 mTorr) | 60 | [62] |
| $SiO_2$ | Ga (30 keV) | $Cl_2$ (1.5 μTorr) | 1.7 | [56] |
| $SiO_2$ | Ga (25 keV) | $H_2O$ (70 mTorr) | 0.2 | [58] |
| $SiO_2$ | Ga (20 keV) | $XeF_2$ (2 Torr) | 8–10 | [63] |
| $Si_2N_4$ | Ar (50 keV) | $XeF_2$ (20 mTorr) | 40 | [62] |
| W | Ga (20 keV) | $XeF_2$ (2 Torr) | 15–75 | [63] |

[a] PMMA = poly(methyl methacrylate).

### 6.4. Other Related Factors

The amount of redeposition in FIBAE is much less than that of milling. Since the products of the gas-assisted etching reaction are volatile and can be easily removed by the FIB pumping system, they are not likely to stick or redeposit to the etched surface or substrate. Depending on the conditions, some of the neutral species may redeposit close to the area of milling, but at a very low rate. Redeposition can be avoided or greatly reduced. The absence of redeposition permits the etching of deep structures with a higher aspect ratio on the order of 10 as compared with ion milling (on the order of one). Another important advantage is the ability to cut metal lines without creating a conductive path through the redeposited metal.[55]

The selectivity is also important in FIBAE. Because FIBAE is essentially a chemical process, it discriminates between materials. For example, in silicon-based semiconductor processing, $XeF_2$ enhances the etching of Si, $SiO_2$, and W but does not enhance Al removal, while $Cl_2$ only increases the etch rate for Si and Al. This selectivity is essential for selectively removing one material in a multilayer structure. The material on top can be rapidly etched with a precursor gas only selective to this material and the removal rate will drop sharply once the lower layer is reached. Young et al. have reported the typical selectivities between materials obtained by FIB milling and FIBAE, in which the selectivity is defined as the ratio of the relevant etch rates for the two materials under the same etching conditions.[56]

## 7. Concluding Remarks

The recent developments in focused ion beam (FIB) technology for nanofabrication have been studied. In general, the recent technology has been rapidly developing to produce more complicated nanoscale structures necessary in various fields. The essence of FIB nanofabrication is the ability to operate an FIB with a proper beam size, current, and energy to remove or add a required amount of materials at the nanometer level from a predefined location in a controllable manner. Consequently, the system equipment has to be improved with an ultra-precision stage and loading operations under a controlled environment, including the direction and position of the ion beam on the target synchronizing with substrate movement, as well as with the chemical feeding instruments for deposition and etching. The accuracy of the substrate stage to perform translation and rotation should be within sub-nanometer ranges with respect to the target position of the ion beams.

To achieve near-atomic-scale accuracy, it is inevitable to have a feedback system to control the material removal rate or deposition rate. A feedback signal that detects or monitors the fabricated dimensions in sub-nanoscale accuracy during operation becomes a necessity. A reliable FIB system with the capability for end-point detection or in situ monitoring should be developed further, especially to improve the quality of these online inspection or monitoring techniques, which include scanning electron microscopy, scanning ion microscopy, and secondary-ion mass microscopy. It has been found that the feedback system in the current commercially available FIB system is still in its infant stage. Other product qualities, such as flatness, texture, and surface finish, can also be important in many applications, and further investigation and development of the in situ detection systems will also be worthwhile.

It is believed that FIB technology will play a major role in nanofabrication because of its combined superiority in flexibility, resolution, precision, and cost, and because of its combined ability for material addition (deposition and implantation) and removal (milling and etching). Among the four techniques in FIB direct writing (milling, implantation, induced deposition, and assisted etching), FIBAE is the most efficient and its processing rate is about one order of magnitude faster than the other three processes. Currently,

  

however, the material removal rate of FIBAE may be too large or unstable to be controlled within the required subnanoscale levels. As a result, a better precision in control of the material removal is needed for FIBAE to be suitable for nanofabrication. Furthermore, although the four FIB-related processes are all used in the semiconductor industry for different applications, these FIB techniques, especially FIBID and FIBAE, have been developed for a limited number of materials directly related to IC fabrication. For example, no etch or deposition chemicals have been reported for effective etching or deposition for most metal oxide compounds used in superconductors or ferroelectrics. More effective chemicals suitable for FIBID and FIBAE should be developed to extend their applications.

In milling, the effects of sputtering, redeposition, and amorphization are all important and have to be understood for enabling better control over the process. For example, the volume yield due to amorphization can be much higher than that of milling, which can certainly deteriorate the dimensional accuracy of nanoscale fabrication. Currently, if the throughput is not the issue, an ultrasmall amount of materials can be milled from the substrate using extremely small beam diameters (on the order of 10 nm) and currents (on the order of 1 pA). Furthermore, if no information is available on the milling of special materials and structures, it can be roughly assumed that the milling yield is close to the value of the normal-incident sputtering yield. This is because several studies have shown that the effect of redeposition often counterbalances the increase in milling yield due to changing the incident angle.

One of the common challenges for all the direct-writing techniques is to downscale the feature size while maintaining a high throughput. To increase the throughput and the ability for use in production, the writing rate of the existing systems has to be improved. A variable-diameter beam system should be developed to provide multiresolution writing to cope with different accuracy or tolerance requirements. It would be ideal if the beam diameter could be continuously changed in situ. This type of system has been available for many macroscale fabrication processes.[57] With this system, a larger beam can be used for roughing 'cut'-(writing) to increase the writing rate in regions where only a lower resolution is needed. Once the two-beam system with improved automation is developed, it will be a significant candidate for becoming the mainstream tool in future nanofabrication industry. Eventually, in the post-nanofabrication or post-miniaturization era, the nano, micro, and macro approaches will have to cross each others boundaries, that is, if nanofabrication is to be successful, it has to be possible to integrate it with its counterparts in the micro and macro regimes, and vice versa.

## Acknowledgements

*The author gratefully acknowledges the financial support for this study by the US National Science Foundation under Grant Nos. DMI-0002466, CMS-0115828, and DMI-0423457, and by Pacific Technology of Arizona. For information and encouragement in preparing this manuscript, Prof. Khalil Arshak of the University of Limerick (Ireland), Prof. Jürgen Brugger of the Swiss Federal Institute of Technology (Switzerland), Prof. Shinji Matsui and Dr. Takahiko Morita of the Himeji Institute of Technology (Japan), and Profs. Zhao-Ying Zhou and Xiong-Ying Ye of Tsinghua University (China) are specifically acknowledged.*

[1] A. A. Tseng, K. Chen, C. D. Chen, and K. J. Ma, *IEEE Trans. Electron. Packag. Manuf.* **2003**, *26*, 141–149.
[2] R. Gerlach, M. Utlaut, "Focused ion beam methods of nanofabrication: room at the bottom, " in *Charged Particle Detection, Diagnostics, and Imaging, Vol. 4510*, Proceedings of SPIE, Int. Society for Optical Eng. **2001**, pp. 96–106.
[3] J. Melngailis, "Applications of ion microbeam lithography and direct processing, " in *Handbook of VLSI Lithography*, 2nd ed. (Ed.: J. N. Helbert), Noyes, Park Ridge, NJ, **2001**, pp. 791–855.
[4] A. A. Tseng, *J. Micromech. Microeng.* **2004**, *14*, R15–R34.
[5] A. A. Tseng, "Recent Developments in Nanofabrication using Ion Projection Lithography", *Small* **2005**, *1*, 594–608.
[6] K. Edinger, "Focused ion beams for direct writing, " in *Direct-Write Technologies for Rapid Prototyping Applications: Sensors, Electronics, and Integrated Power Sources* (Eds.: A. Pique, D. B. Chrisey), Academic Press, San Diego, CA, **2002**, pp. 347–383.
[7] S. Reyntjens, R. Puers, *J. Micromech. Microeng.* **2001**, *11*, 287–300.
[8] J. P. Biersack, L. G. Haggmark, *Nucl. Instrum. Methods Phys. Res. Sect. B* **1980**, *174*, 257–269.
[9] J. F. Zeigler, J. P. Biersack, U. Littmark, *The Stopping Range of Ions in Solids*, Pergamon, New York, NY, **1985**.
[10] L. Frey, C. Lehrer, H. Ryssel, *Appl. Phys. A* **2003**, *76*, 1017–1023.
[11] A. Lugstein, B. Basnar, J. Smoliner, E. Bertagnolli, *Appl. Phys. A* **2003**, *76*, 545–548.
[12] J. S. Custer, M. O. Thompson, D. C. Jacobson, J. M. Poate, S. Roorda, W. C. Sinke, F. Spaepen, *Appl. Phys. Lett.* **1994**, *64*, 437–439.
[13] H. W. Li, D. J. Kang, M. G. Blamire, W. T. S. Huck, *Nanotechnology* **2003**, *14*, 220–223.
[14] J. L. Wilbur, G. M. Whitesides, "Self-Assembly and Self-Assembled Monolayers in Micro and Nanofabrication" in *Nanotech.* (Ed.: G. Timp), Chapter 8, Springer, New York, NY, **1999**, pp. 331–368.
[15] A. A. Tseng, A. Notargiacomo, *J. Nanosci. Nanotechnol.* **2005**, *5*, 683–702.
[16] P. Grabiec, J. Radojewski, M. Zaborowski, K. Domanski, T. Schenkel, I. W. Rangelow, *J. Vac. Sci. Technol. B* **2004**, *22*, 16–21.
[17] S. Ohkouchi, Y. Nakamura, H. Nakamura, K. Asakawa, *Thin Solid Films* **2004**, *464–465*, 233–236.
[18] A. A. Tseng, I. A. Insua, J. S. Park, B. Li, G. P. Vakanas, *J. Vac. Sci. Technol. B* **2004**, *22*, 82–89.
[19] A. A. Tseng, B. Leeladharan, B. Li, I. A. Insua, C. D. Chen, *Int. J. Nanosci.* **2003**, *2*, 375–379.
[20] R. Menzel, T. Bachmann, F. Machalett, W. Wesch, U. Lang, M. Wendt, C. Musil, R. Mühle, *Appl. Surf. Sci.* **1998**, *136*, 1–7.
[21] Y. K. Park, F. Pászti, M. Takai, C. Lehrer, L. Frey, H. Ryssel, "Comparison of FIB-Induced Physical and Chemical Etching" in *Proc. Inter. Conf. Ion Implantation, Vol. 2*, IEEE, **1999**, pp. 820–823.
[22] G. Xiong, D. A. Allwood, M. D. Cooke, R. P. Cowburn, *Appl. Phys. Lett.* **2001**, *79*, 3461–3463.
[23] B. D. Huey, R. M. Langford, *Nanotechnology* **2003**, *14*, 409–412.
[24] A. Stanishevsky, *Diamond Relat. Mater.* **1999**, *8*, 1246–1250.

  

[25] A. Lugstein, B. Basnar, G. Hobler, E. Bertagnolli, *J. Appl. Phys.* **2002**, *92*, 4037 – 4042.
[26] S.-J. Kim, Y. I. Latyshev, T. Yamashta, *Appl. Phys. Lett.* **1999**, *74*, 1156 – 1158.
[27] T. Nagase, T. Kubota, S. Mashiko, *Thin Solid Films* **2003**, *438–439*, 374 – 377.
[28] A. J. Steckl, H. C. Mogul, S. Mogren, *Appl. Phys. Lett.* **1992**, *60*, 1833 – 1835.
[29] J. Brugger, G. Beljakovic, M. Despont, M. N. F. de Rooij, P. Vettiger, *Microelectron. Eng.* **1997**, *35*, 401 – 404.
[30] J. Xu, A. J. Steckl, *Appl. Phys. Lett.* **1994**, *65*, 2081 – 2083.
[31] T. Hiramoto, K. Hirakawa, T. Ikoma, *J. Vac. Sci. Technol. B* **1988**, *6*, 1014 – 1017.
[32] D.-J. Bai, Y.-Q. Zhang, A. Matsushita, A. Baba, A. Kenjo, T. Sadoh, H. Nakashima, H. Mori, T. Tsurushima in *Proc. Inter. Conf. Ion Implantation, Vol. 2*, IEEE, **1999**, 1101 – 1104.
[33] B. Prevel, L. Bardotti, S. Fanget, A. Hannour, P. Melinon, A. Perez, J. Gierak, G. Faini, E. Bourhis, D. Mailly, *Appl. Surf. Sci.* **2004**, *226*, 173 – 177.
[34] K. Arshak, M. Mihov, A. Arshak, D. McDonagh, D. Sutton, *Microelectron. Eng.* **2004**, *73–74*, 144 – 151.
[35] T. Sumita, T. Nagai, H. Kubota, T. Matsukawa, I. Ohdomari, *Synth. Met.* **1999**, *103*, 2234 – 2237.
[36] S. Kalbitzer, *Curr. Opin. Solid State Mater. Sci.* **2002**, *6*, 271 – 279.
[37] S. Khizroev, D. Litvinov, *Nanotechnology* **2004**, *15*, R7 – R15.
[38] H. Ryssel, I. Ruge, *Ion Implantation*, John Wiley & Sons, New York, NY, **1986**.
[39] M. J. Madou, *Fundamentals of Microfabrication: The Science of Miniaturization*, 2nd ed., CRC Press, Boca Raton, FL, **2002**.
[40] T. Shinada, H. Koyama, C. Hinoshita, K. Imamura, I. Ohdomari, *Jpn. J. Appl. Phys.* **2002**, *41*, L287 – L290.
[41] S. Matsui, T. Kaito, J. Fujita, M. Komuro, K. Kanda, Y. Haruyama, *J. Vac. Sci. Technol. B* **2000**, *18*, 3181 – 3184.
[42] L. R. Harriott, M. J. Vasile, *J. Vac. Sci. Technol. B* **1988**, *6*, 1035 – 1038.
[43] K. Edinger, J. Melngailis, J. Orloff, *J. Vac. Sci. Technol. B* **1998**, *16*, 3311 – 3314.
[44] K. A. Telari, B. R. Rogers, H. Fang, L. Shen, R. A. Weller, D. N. Braski, *J. Vac. Sci. Technol. B* **2002**, *20*, 590 – 595.
[45] T. Morita, R. Kometani, K. Watanabe, K. Kanda, Y. Haruyama, T. Hoshino, K. Kondo, T. Kaito, T. Ichihashi, J. Fujita, M. Ishida, Y. Ochiai, T. Tajima, S. Matsui, *J. Vac. Sci. Technol. B* **2003**, *21*, 2737 – 2741.
[46] S. M. Allameha, N. Yao, W. O. Soboyejo, *Scripta Mater.* **2004**, *50*, 915 – 919.
[47] K. Watanabe, T. Morita, R. Kometani, T. Hoshino, K. Kondo, K. Kanda, Y. Haruyama, T. Kaito, J. Fujita, M. Ishida, Y. Ochiai, T. Tajima, S. Matsui, *J. Vac. Sci. Technol. B* **2004**, *22*, 22 – 26.
[48] J.-F. Lin, J. P. Bird, L. Rotkina, P. A. Bennett, *Appl. Phys. Lett.* **2003**, *82*, 802 – 804.
[49] H. Langfischer, B. Basnar, H. Hutter, E. Bertagnolli, *J. Vac. Sci. Technol. B* **2002**, *20*, 1408 – 1415.
[50] K. Edinger, *J. Vac. Sci. Technol. B* **1999**, *17*, 3058 – 3062.
[51] J. D. Casey, Jr., M. Phaneuf, K. E. Noll, R. Schuman, T. J. Gannon, A. Krechmer, D. Monforte, N. Antoniou, N. Bassom, J. Li, P. Carleson, C. Huynh, *J. Vac. Sci. Technol. B* **2002**, *20*, 2682 – 2685.
[52] J. Taniguchi, N. Ohno, S. Takeda, I. Miyamoto, M. Komuro, *J. Vac. Sci. Technol. B* **1998**, *16*, 2506 – 2510.
[53] D. P. Adams, M. J. Vasile, T. M. Mayer, V. C. Hodges, *J. Vac. Sci. Technol. B* **2003**, *21*, 2334 – 2343.
[54] A. Stanishevsky, *Thin Solid Films* **2001**, *398–399*, 560 – 565.
[55] J. Orloff, *Rev. Sci. Instrum.* **1993**, *64*, 1105 – 1130.
[56] R. J. Young, J. R. A. Cleaver, H. Ahmed, *J. Vac. Sci. Technol. B* **1993**, *11*, 234 – 241.
[57] A. A. Tseng, M. Tanaka, *Rapid Prototyping J.* **2001**, *7*, 6 – 17.
[58] T. J. Stark, G. M. Shedd, J. Vitarelli, D. P. Griffis, P. E. Russell, *J. Vac. Sci. Technol. B* **1995**, *13*, 2565 – 2569.
[59] I. Chyr, A. J. Steckl, *J. Vac. Sci. Technol. B* **2001**, *19*, 2547 – 2550.
[60] Y. Ochiai, K. Gamo, S. Namba, K. Shihoyama, A. Masuyama, T. Shiokawa, K. Toyoda, *J. Vac. Sci. Technol. B* **1987**, *5*, 423 – 426.
[61] A. Yamaguchi, T. Nishikawa, *J. Vac. Sci. Technol. B* **1995**, *13*, 962 – 966.
[62] Z. Xu, K. Gamo, S. Namba, *J. Vac. Sci. Technol. B* **1988**, *6*, 1039 – 1042.
[63] L. R. Harriott, *J. Vac. Sci. Technol. B* **1993**, *11*, 2012 – 2015.

Received: April 2, 2005
Published online on August 18, 2005

  